

Cation Exchange as a Mechanism to Engineer Polarity in Layered Perovskites.

Tong Zhu[†], Guru Khalsa[¶], Dana M. Havas[¶], Alexandra S. Gibbs[‡], Weiguo Zhang[§], P. Shiv Halasyamani[§], Nicole A. Benedek^{¶*} and Michael A. Hayward^{†*}

[†] Department of Chemistry, University of Oxford, Inorganic Chemistry Laboratory, South Parks Road, Oxford, OX1 3QR, UK.

[¶] Department of Materials Science and Engineering, Cornell University, Ithaca, New York 14853, USA.

[‡] ISIS Facility, Rutherford Appleton Laboratory, Chilton, Oxon OX11 0QX, UK.

[§] Department of Chemistry, University of Houston, 112 Fleming Building, Houston, Texas 77204-5003, USA.

Cation exchange reactions performed on the $n = 2$ Dion-Jacobson phases $\text{RbNdNb}_2\text{O}_7$ and $\text{RbNdTa}_2\text{O}_7$, using LiNO_3 and NaNO_3 , yield the corresponding LiNdM_2O_7 and NaNM_2O_7 ($M = \text{Nb, Ta}$) phases. Synchrotron X-ray and neutron powder diffraction data, in combination with second-harmonic generation data and supported by first-principles DFT calculations, reveal that the LiNdM_2O_7 phases adopt $n = 2$ Ruddlesden-Popper type structures with an $a^-a^-c^+/(a^-a^-c^-)$ distortion described in the polar space group $B2cm$. In contrast, the NaNM_2O_7 phases adopt $n = 2$ Ruddlesden-Popper type structures with an $a^-b^0c^0/b^0a^-c^0$ distortion, described in the centrosymmetric space group $P4_2/mnm$. The differing structures adopted by the LiNdM_2O_7 and NaNM_2O_7 phases are rationalized on the basis of a competition between i) optimizing the size of the Li/Na coordination site via octahedral tilting and ii) ordering the Na/Li cations within the (Li/Na) O_2 sheets to minimize cation-cation repulsion – the former appears to be the dominant factor for the Li phases and the latter factor dominates for the Na phases. The strong A'-cation dependence of the tilting distortions adopted by the $\text{A}'\text{NdM}_2\text{O}_7$ phases suggests that by careful selection of the substituting cation the tilting distortions of layered perovskite phases can be rationally tuned to adopt polar configurations, and thus new ferroelectric phases can be synthesized.

Introduction

Ferroelectric materials – those which exhibit a spontaneous, switchable electrical polarization – are utilized in a wide variety of technical applications.¹ However the discovery and design of new ferroelectric materials is challenging because a prerequisite for a material to exhibit ferroelectric behavior is the adoption of a non-centrosymmetric (NCS) polar crystal structure.²⁻³ This is a taxing requirement because, in general, symmetric packing schemes are more efficient than asymmetric arrangements, and thus NCS structures tend to be energetically disfavored compared to centrosymmetric alternatives.

The most common approach used to try to stabilize NCS structures is the exploitation of second-order Jahn-Teller (SOJT) distortions to break symmetry locally. For example, by including either octahedrally coordinated d^0 transition metal cations (e.g. Ti^{4+} in BaTiO_3)⁴⁻⁷ or post-transition elements with ns^2 electronic configurations (e.g. Bi^{3+} in BiFeO_3)⁸⁻¹³ SOJT interactions can be used to favor NCS structures. However this route restricts which elements can be included in ferroelectric materials, and is especially limiting if the desire is to combine ferroelectricity with ferromagnetism to prepare magnetoelectric multiferroic materials.¹⁴

Recently theoretical analysis has been used to develop a strategy of harnessing the collective tilts and rotations of the octahedral units in perovskite phases and their layered analogues to break inversion symmetry.¹⁵⁻¹⁷ By combining two non-polar distortion modes (typically rotations around the x - and y -axes combined with rotations around the z -axis) a third polar distortion mode becomes allowed *via* the ‘tri-linear’

coupling mechanism.^{15, 18} Thus the inversion symmetry of the centrosymmetric aristotype structure can be lifted by harnessing common, low-energy structural distortions, without the need to include any special chemical elements. This insight provides a rational pathway by which NCS structures can be stabilized and ferroelectric behavior induced, because the tilting distortions of perovskite lattices and their layered analogues can be controlled through simple packing effects arising from the sizes of the ions which make up a phase.¹⁹⁻²¹ A number of studies have demonstrated this behavior experimentally, most notably in the $\text{A}_3\text{B}_2\text{O}_7$ $n = 2$ Ruddlesden-Popper structure where $(\text{Ca,Sr})_3\text{Ti}_2\text{O}_7$,²² $\text{Ca}_3\text{Mn}_2\text{O}_7$,²³ and $\text{Sr}_3\text{Zr}_2\text{O}_7$ ²⁴ have been shown to not only adopt NCS structures, but also ferroelectric behavior.

The tri-linear mechanism for symmetry breaking is not limited to the $n = 2$ Ruddlesden-Popper framework. Recently it has been shown that it can also operate in the $\text{A}'\text{AB}_2\text{O}_7$ Dion-Jacobson phases,²⁵⁻²⁶ leading to a series of polar, potentially ferroelectric materials.²⁷⁻²⁹ An additional feature of the Dion-Jacobson phases is that they exhibit a wide variety of cation exchange reactions³⁰⁻³² in which the monovalent A' cation (typically Rb^+ or Cs^+) can be exchanged for a broad range of other cations,³³⁻³⁶ metal salts³⁷⁻³⁹ or complex molecules⁴⁰⁻⁴² to yield phases which are often metastable and unpreparable by more direct routes. This diverse cation exchange chemistry offers a simple method to tune the tilting distortions of the Dion-Jacobson lattice and hence induce ferroelectric behavior.

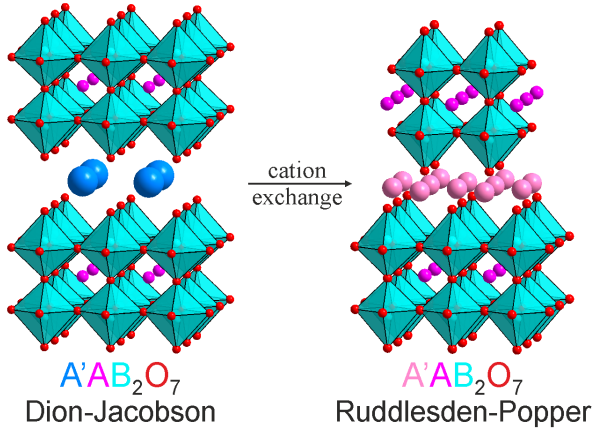


Figure 1. The structural transformation when an $A'AB_2O_7$ ($A' = \text{Rb}, \text{Cs}$) Dion-Jacobson phase is converted into an $A'AB_2O_7$ ($A' = \text{Li}, \text{Na}$) Ruddlesden-Popper phase. In the latter structure the pink A' cation sites are 50% occupied.

The simple like-for-like exchange of monovalent cations in Dion-Jacobson phases has been extensively studied and it has been observed that when the large A' cations (Rb^+ or Cs^+ for example) within the lattice are exchanged for smaller cations, such as Li^+ or Na^+ , the AB_2O_7 double perovskite sheets change their stacking arrangement from a simple ‘primitive’ stacking to the ‘body-centered’ stacking of the Ruddlesden-Popper framework. This shifting of the perovskite sheets creates a series of 4-fold, pseudo tetrahedral inter-layer coordination sites in which the small Li^+ and Na^+ cations reside, as shown in Figure 1.^{33, 35, 43} Here we describe the detailed structural characterization of LiNdM_2O_7 and NaNdM_2O_7 ($M = \text{Nb}, \text{Ta}$) prepared *via* the cation exchange of the corresponding RbNdM_2O_7 phase, and show in contrast to previous reports that both the lithium and sodium phases adopt distorted structures, with the lithium phases adopting NCS polar structures.

Experimental

Synthesis. Samples of $\text{RbNdNb}_2\text{O}_7$ and $\text{RbNdTa}_2\text{O}_7$ were prepared from Rb_2CO_3 (99.8%), Nd_2O_3 (99.99%, dried at 900 °C) and Nb_2O_5 (99.9985%, dried at 900 °C) or Ta_2O_5 (99.993%, dried at 900 °C) as described previously.²⁸ Suitable stoichiometric ratios of the oxides were ground together in an agate pestle and mortar and then combined with a 50% excess of Rb_2CO_3 (to compensate for metal loss due to volatility at high temperature). These mixtures were then heated at 850 °C in air for 12 h, reground, and pressed into pellets. Samples of $\text{RbNdNb}_2\text{O}_7$ were heated in air for four periods of 48 h at 1000 °C and a further 48 h at 1050 °C. Samples of $\text{RbNdTa}_2\text{O}_7$ were heated in air for four periods of 48 h at 1050 °C. All samples were reground and pressed into pellets between heating cycles. After heating, all samples were washed with distilled water to remove any remaining excess rubidium oxide, and then dried for 12 h at 140 °C in air.

Lithium and sodium cation-exchange reactions were performed by reacting $\text{RbNdNb}_2\text{O}_7$ and $\text{RbNdTa}_2\text{O}_7$ with 10 mole-equivalents of either LiNO_3 (99.98%) or NaNO_3 (>99.0%). These mixtures were ground together and loaded into an open ended silica tube. Lithium exchange reactions were heated in air for two periods of 48 h at 300 °C. Sodium exchange reactions were heated in air for two periods of 48 h at 400 °C. Reaction vessels were kept in a vertical orientation during the heating cycles as both lithium and sodium nitrate melt at the applied reaction temperatures. Between heating cycles, samples were washed with distilled water, dried for 12

h at 140 °C in air and mixed with a further 10 mole-equivalents of lithium or sodium nitrate. After the final heating step, all samples were washed with distilled water to remove remaining lithium or sodium nitrate, and dried for 12 h at 140 °C in air. Samples of $\text{NaNdNb}_2\text{O}_7$ and $\text{NaNdT}_a_2\text{O}_7$ then dried under flowing argon for 12 h at 300 °C to eliminate all water and then transferred into an Argon-filled glove box for storage.

Characterization. Reaction progress and final sample purity were assessed using X-ray powder diffraction data collected using a PANalytical X’pert diffractometer incorporating an X’celerator position sensitive detector (monochromatic $\text{Cu K}\alpha 1$ radiation). High-resolution synchrotron X-ray powder diffraction data were collected using instrument I11 at Diamond Light Source Ltd. Diffraction patterns were measured using Si-calibrated X-rays with an approximate wavelength of 0.825 Å, from samples sealed in 0.3 mm diameter borosilicate glass capillaries. Neutron powder diffraction data were collected from samples contained within vanadium cans, using the HRPD diffractometer at the ISIS neutron source. Rietveld profile refinement was performed using the GSAS suite of programs.⁴⁴

The particle-size dependent second harmonic generation (SHG) response of samples was measured by grinding sintered pellets of material and then sieving the resulting powders into distinct particle size ranges (<20, 20-45, 45-63, 63-75, 75-90, 90-25 µm). SHG intensity was then recorded from each particle size range and compared to a standard sample of $\alpha\text{-SiO}_2$ in the same particle size ranges. No index matching fluid was used in any of the experiments. A detailed description of the experimental setup and process has been reported previously.⁴⁵

First-Principles Calculations. The first-principles calculations were performed using the PBEsol exchange-correlation functional⁴⁶ and projector augmented wave (PAW) pseudopotentials,⁴⁷⁻⁴⁸ as implemented in the VASP package.⁴⁹⁻⁵² The valence electron configurations for each pseudopotential were as follows: $\text{Li} - 1s^2 2s^1$, $\text{Na} - 2s^2 3s^1 2p^6$, $\text{Nd} - 5s^2 6s^2 5p^6 5d^1$, $\text{Nb} - 4s^2 5s^1 4p^6 4d^4$, $\text{Ta} - 5p^6 5d^4 6s^1$, and $\text{O} - 2s^2 2p^4$. Good convergence of structural parameters (lattice parameters and Wyckoff positions) was achieved for a plane wave cutoff of 700 eV and a $6 \times 6 \times 2$ Monkhorst-Pack mesh, compared to higher plane wave cutoffs and denser k-point meshes. Structural relaxations were considered converged when the force on each atom became smaller than 1 meV/Å.

Results

Structural Characterization of $\text{LiNdNb}_2\text{O}_7$ and $\text{LiNdTa}_2\text{O}_7$. Synchrotron X-ray and neutron powder diffraction data collected from $\text{LiNdNb}_2\text{O}_7$ and $\text{LiNdTa}_2\text{O}_7$ can be indexed using orthorhombic unit cells ($\text{LiNdNb}_2\text{O}_7$: $a = 5.450$ Å, $b = 5.397$ Å, $c = 20.455$ Å; $\text{LiNdTa}_2\text{O}_7$: $a = 5.443$ Å, $b = 5.409$ Å, $c = 20.501$ Å) consistent with distorted $n = 2$ Ruddlesden-Popper type structures. This contrasts previous reports of an undistorted ($I4/mmm$) structure for $\text{LiNdNb}_2\text{O}_7$.³⁵ We did not observe any evidence by diffraction for mixed cation (Li/Rb) NdNb_2O_7 or (Li/Rb) NdTa_2O_7 phases during the cation exchange reactions, with RbNdM_2O_7 starting materials converting directly to LiNdM_2O_7 product phases.

Directly determining the distortion adopted by an $n = 2$ Ruddlesden-Popper phase can be challenging from powder diffraction data. To assist us, we have built on the work of Aleksandrov and Bartolome⁵³ (who listed all the mathematically possible distortions of the $n = 2$ Ruddlesden-Popper framework) by performing a symmetry analysis using

space group	tilt system	Glazer tilt	χ^2	wRp (%)	Rp (%)
LiNdNb ₂ O ₇					
<i>P2₁nm</i>	$\Phi_1\Phi_2\Psi_z/\Phi_2\Phi_1\Psi_z$	$a^-b^-c^+/b^-a^-c^+$	111.3	16.18	13.35
<i>P2cm</i>	$\Phi_1\Phi_2\Psi_z/-(\Phi_1\Phi_2)\Psi_z$	$a^-b^-c^+/-(a^-b^-)c^+$	10.10	4.88	5.61
<i>P2cm</i> (constrained)	$\Phi_1\Phi_2\Psi_z/-(\Phi_1\Phi_2)\Psi_z$	$a^-b^-c^+/-(a^-b^-)c^+$	17.79	6.48	6.52
<i>B2cm</i>	$\Phi\Phi\Psi_z/-(\Phi_1\Phi_2\Psi_z)$	$a^-a^-c^+/-(a^-a^-)c^+$	12.78	5.49	6.04
LiNdTa ₂ O ₇					
<i>P2₁nm</i>	$\Phi_1\Phi_2\Psi_z/\Phi_2\Phi_1\Psi_z$	$a^-b^-c^+/b^-a^-c^+$	83.51	14.41	13.66
<i>P2cm</i>	$\Phi_1\Phi_2\Psi_z/-(\Phi_1\Phi_2)\Psi_z$	$a^-b^-c^+/-(a^-b^-)c^+$	4.57	3.37	4.02
<i>P2cm</i> (constrained)	$\Phi_1\Phi_2\Psi_z/-(\Phi_1\Phi_2)\Psi_z$	$a^-b^-c^+/-(a^-b^-)c^+$	8.52	4.61	4.73
<i>B2cm</i>	$\Phi\Phi\Psi_z/-(\Phi_1\Phi_2\Psi_z)$	$a^-a^-c^+/-(a^-a^-)c^+$	5.76	3.79	4.38

Table 1: Fitting Statistics from the structural refinement of LiNdNb₂O₇ and LiNdTa₂O₇ against neutron powder diffraction data.

the ISODISTORT software⁵⁴ to produce a list of the ‘chemically plausible’ distortions of the framework, listed in Table S1 in the supporting information. We define the ‘chemically plausible’ distortions as those that retain equivalence of all the BO₆ octahedra in the framework, and we have henceforth assumed that LiNdNb₂O₇ and LiNdTa₂O₇ adopt one of the distorted structures listed in Table S1. For ease of comparison we will describe all distorted structures using unit cells in which the stacking direction is aligned parallel to the z-axis (column 5 in Table S1).

Particle-size dependent SHG data, shown in Figure 2, indicate that both LiNdNb₂O₇ and LiNdTa₂O₇ are SHG active, and thus adopt non-centrosymmetric crystal structures. This information allows us to eliminate all of the centrosymmetric structures in Table S1, leaving 4 non-centrosymmetric candidate space groups: *Bb2₁m*, *P2₁nm*, *B2cm* and *P2cm*. Further examination of the diffraction data allowed us to eliminate the *Bb2₁m* structural models on the basis of extinction conditions, as described in Figure S1 in Supporting Information, to leave 3 candidate structures.

Structural models were constructed for LiNdNb₂O₇ and LiNdTa₂O₇ in space groups *P2₁nm*, *B2cm* and *P2cm*. The lithium cations reside in 4-coordinate, pseudo-tetrahedral sites located between the perovskite double-layers of the phase. As there are twice as many of these sites in the aristotype structure than are required to satisfy the LiNdM₂O₇ stoichiometry, it is possible to arrange the lithium cations in either ordered or disordered configurations. The structural model in space group *P2₁nm* locates the lithium coordination positions on two separate 4b crystallographic sites. The model in space group *P2cm* has two 2a and two 2b sites while in space group *B2cm* there is one 4a and one 4b site to describe the 4-coordinate lithium sites. As a result the lithium cations can adopt a variety of ordered or disordered arrangements in these models.

Refinement of the three remaining candidate models against the neutron powder diffraction data proceeded smoothly for both phases. During the refinements all atomic positional and displacement parameters were refined freely and the occupancies of the lithium sites were also refined (within the constraint of the overall sample stoichiometry) to determine if the lithium cations were ordered or disordered. It was observed that ordered lithium configurations gave superior fits for both the *P2cm* and *B2cm* models while in the *P2₁nm* model with a disordered lithium configuration gave a better fit than an ordered configuration.

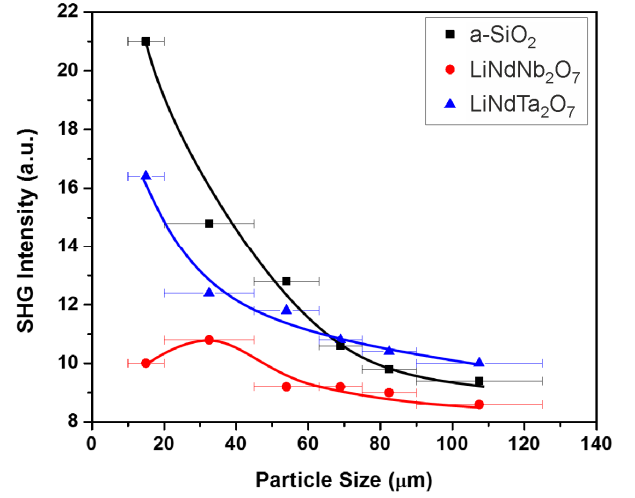


Figure 2. Plot of SHG activity of LiNdNb₂O₇ and LiNdTa₂O₇ as a function of particle size, compared to that of an α -SiO₂ standard.

Fitting statistics for the three structural models reveal that for both LiNdNb₂O₇ and LiNdTa₂O₇ the *P2cm* and *B2cm* models give far superior fits to the data than the lithium-disordered *P2₁nm* model (Table 1), however the difference between the quality of the fits for the ‘unconstrained *P2cm*’ and *B2cm* models is too small to pick a ‘correct’ structural solution.

Close examination of the refined structures from ‘unconstrained’ *P2cm* models reveals they are very irregular. The *P2cm* model has 2 Li, 2 Nd, 2 Nb/Ta and 8 oxide ions in the asymmetric unit - twice as many as the *B2cm* model. This lower symmetry allows the model to yield a structure in which chemically equivalent atoms reside in different local environments. As a result bond valence sums (BVS)⁵⁵⁻⁵⁶ calculated for the pairs of chemically equivalent cations (listed in Table S2, in the Supporting Information) are very uneven for the ‘unconstrained *P2cm*’ model, breaking the chemical plausibility criterion described above. To address this situation, we added constraints to the *P2cm* model to make the pairs of cation sites more equivalent. This more symmetric model (labelled *P2cm*_(constrained)) fitted the data much more poorly than the *B2cm* model, as shown in Table 1, indicating that the $a^-b^-c^+/-(a^-b^-)c^+$ distortion of the *P2cm* model is incorrect and

Atom	site	x	y	z	U _{iso} (Å ³)
Li(1)	4a	0.5820(20) <i>0.56127</i>	0 <i>0</i>	½ <i>½</i>	0.0294(22)
Nd(1)	4c	0.2957(8) <i>0.28281</i>	0.2520(5) <i>0.24873</i>	¼ <i>¼</i>	0.0161(6)
Nb(1)	8d	0.3136(7) <i>0.31942</i>	0.7518(4) <i>0.75086</i>	0.1390(1) <i>0.13948</i>	0.0162(4)
O(1)	8d	0.3101(8) <i>0.31082</i>	0.8386(3) <i>0.84089</i>	0.0566(1) <i>0.05598</i>	0.0172(5)
O(2)	8d	0.1225(5) <i>0.12826</i>	0.4556(5) <i>0.44969</i>	0.1443(1) <i>0.14445</i>	0.0216(6)
O(3)	8d	0.5598(6) <i>0.55002</i>	0.0154(7) <i>0.03124</i>	0.1719(1) <i>0.17302</i>	0.0227(6)
O(4)	4c	0.3195(10) <i>0.34469</i>	0.6819(5) <i>0.67719</i>	¼ <i>¼</i>	0.0201(8)

LiNdNb₂O₇ – space group *B2cm* (#39)
Lattice parameters from experiment:
 $a = 5.4498(2)$ Å, $b = 5.3974(2)$ Å, $c = 20.4556(8)$ Å,
volume = 601.70(7) Å³
Lattice parameters from theory:
 $a = 5.43799$ Å, $b = 5.37584$ Å, $c = 20.47048$ Å,
volume = 598.43 Å³
Formula weight: 448.99 g mol⁻¹, Z = 4
Radiation source: Neutron Time of flight
Temperature: 298 K
 $\chi^2 = 12.78$, wRp = 5.49%, Rp = 6.04%

Table 2. Parameters from the structural refinement of LiNdNb₂O₇ against neutron powder diffraction data collected at 298 K compared to structural data from our first-principles calculations. For each atomic species, the first row of fractional coordinates corresponds to experimental data (with the corresponding isotropic displacement parameter), whereas the second row (italic) is from our DFT calculations.

that LiNdNb₂O₇ and LiNdTa₂O₇ adopt $a^-a^-c^+/-(-a^-a^-c^+)$ distorted, *B2cm* symmetry Ruddlesden-Popper structures. Our DFT calculations confirm that a structure with *B2cm* symmetry is more stable than *P2cm*, however the energy difference between the phases is very small (less than 0.05 meV/formula unit). Indeed, the *P2cm* model essentially relaxes to the *B2cm* structure.

Observed, calculated and difference plots from the refinement of *B2cm* symmetry models of LiNdNb₂O₇ and LiNdTa₂O₇ against neutron powder diffraction data are shown in Figures S2 and S3 respectively. Complete descriptions of the refined structures of LiNdNb₂O₇ and LiNdTa₂O₇ are detailed in Tables 2 and 3 respectively, with selected bond lengths in Table 4. Tables 2 and 3 also show that our relaxed computational structures are in excellent agreement with the experimentally refined structures.

Since these Li phases are polar they will exhibit a macroscopic polarization, which if switchable, would make these materials ferroelectric. It is usually reasonably straightforward to calculate the polarization from first principles but this is not the case here. This is because we require a reference paraelectric structure to calculate the polarization, in addition to the polar, distorted structure (we calculate the *change* in polarization upon application of an electric field, and not the polarization itself, since this quantity is ill-defined in a solid). The choice of reference paraelectric structure is not immediately obvious. We could propose a structure with *Bmcm* symmetry (for example) as our paraelectric reference structure, since this space group is connected to *B2cm* by a

Atom	site	x	y	z	U _{iso} (Å ³)
Li(1)	4a	0.5782(16) <i>0.56132</i>	0 <i>0</i>	0 <i>0</i>	0.0235(15)
Nd(1)	4c	0.2994(7) <i>0.28495</i>	0.2547(4) <i>0.25071</i>	¼ <i>¼</i>	0.0132(4)
Ta(1)	8d	0.3178(6) <i>0.32224</i>	0.7540(3) <i>0.75242</i>	0.1397(1) <i>0.13989</i>	0.0108(3)
O(1)	8d	0.3115(7) <i>0.31069</i>	0.8374(2) <i>0.84079</i>	0.0564(1) <i>0.05575</i>	0.0158(4)
O(2)	8d	0.1170(4) <i>0.12507</i>	0.4611(4) <i>0.45247</i>	0.1457(1) <i>0.14523</i>	0.0195(5)
O(3)	8d	0.5563(5) <i>0.55012</i>	0.0182(5) <i>0.02957</i>	0.1721(1) <i>0.17341</i>	0.0155(4)
O(4)	4c	0.3232(8) <i>0.34333</i>	0.6833(3) <i>0.67899</i>	¼ <i>¼</i>	0.0174(6)

LiNdTa₂O₇ – space group *B2cm* (#39)
Lattice parameters from experiment:
 $a = 5.4427(2)$ Å, $b = 5.4092(2)$ Å, $c = 20.5011(7)$ Å,
volume = 603.57(6) Å³
Lattice parameters from theory:
 $a = 5.44156$ Å, $b = 5.38892$ Å, $c = 20.52571$ Å,
volume = 601.90 Å³
Formula weight: 625.07 g mol⁻¹, Z = 4
Radiation source: Neutron Time of flight
Temperature: 298 K
 $\chi^2 = 5.76$, wRp = 3.79%, Rp = 4.38%

Table 3. Parameters from the structural refinement of LiNdTa₂O₇ against neutron powder diffraction data collected at 298 K compared to structural data from our first-principles calculations. For each atomic species, the first row of fractional coordinates corresponds to experimental data (with the corresponding isotropic displacement parameter), whereas the second row (italic) is from our DFT calculations.

Cation	Anion	LiNdNb ₂ O ₇		LiNdTa ₂ O ₇	
		Length (Å)	BVS	Length (Å)	BVS
Li(1)	O(1) × 2	1.909(12)	0.99	1.930(7)	0.98
	O(1) × 2	2.072(13)		2.054(8)	
Nd(1)	O(2) × 2	2.602(4)	3.07	2.609(3)	3.03
	O(2) × 2	3.215(4)		3.150(4)	
	O(3) × 2	2.501(5)		2.479(4)	
	O(3) × 2	2.507(5)		2.546(4)	
	O(4)	2.324(4)		2.322(4)	
	O(4)	2.620(8)		2.613(7)	
	O(4)	2.877(8)		2.871(7)	
	O(4)	3.080(4)		3.094(4)	
Nb/Ta(1)	O(1)	1.751(3)	5.09	1.767(3)	5.18
	O(2)	1.911(5)		1.929(4)	
	O(2)	2.025(5)		2.005(4)	
	O(3)	1.986(6)		1.996(4)	
	O(3)	2.068(5)		2.042(4)	
	O(4)	2.302(2)		2.294(2)	

Table 4. Selected bond lengths from the structures of LiNdNb₂O₇ and LiNdTa₂O₇ refined in space group *B2cm*.

space group	tilt system	Glazer tilt	χ^2	wRp (%)	Rp (%)
NaNbNb ₂ O ₇					
<i>Pnnm</i> #58	$\Phi_1\Phi_20/\Phi_2\Phi_10$	$a^-b^-c^0/b^-a^-c^0$	8.40	4.67	4.68
<i>Pnam</i> #62	$\Phi\Phi\Psi_z/\Phi\Phi-\Psi_z$	$a^-a^-c^+/a^-a^-c^+$	9.97	5.08	5.20
<i>P4₂/mnm</i> #136	$\Phi00/0\Phi0$	$a^-b^0c^0/b^0a^-c^0$	8.86	4.79	4.82
NaNdTa ₂ O ₇					
<i>Pccm</i> #49	$\Phi_1\Phi_20/-(\Phi_2\Phi_1)0$	$a^-b^-c^+/(b^-a^-)c^0$	19.70	6.95	5.31
<i>Pbcm</i> #57	$\Phi\Phi\Psi_z/-(\Phi\Phi)\Psi_z$	$a^-a^-c^+/(a^-a^-)c^+$	16.85	6.42	5.09
<i>Pnnm</i> #58	$\Phi_1\Phi_20/\Phi_2\Phi_10$	$a^-b^-c^0/b^-a^-c^0$	6.30	3.93	3.82
<i>Pnam</i> #62	$\Phi\Phi\Psi_z/\Phi\Phi-\Psi_z$	$a^-a^-c^+/a^-a^-c^+$	5.99	3.83	3.94
<i>P4₂/mcm</i> #132	$\Phi00/0-\Phi0$	$a^-b^0c^0/b^0a^-c^0$	21.78	7.31	5.57
<i>P4₂/mnm</i> #136	$\Phi00/0\Phi0$	$a^-b^0c^0/b^0a^-c^0$	6.96	4.13	3.98

Table 5. Fitting statistics from the structural refinement of NaNbNb₂O₇ and NaNdTa₂O₇ against neutron powder diffraction data.

single distortion that breaks inversion symmetry and transforms like the irreducible representation Γ_4^- . However, if polarization switching actually proceeds through a different structure, then our prediction may be quite poor. Rather than muddy the literature with theoretical results of questionable physical value, we have chosen not to calculate a polarization value in this instance.

Structural Characterization of NaNbNb₂O₇ and NaNdTa₂O₇. Synchrotron X-ray and neutron powder diffraction data collected from NaNbNb₂O₇ and NaNdTa₂O₇ could be indexed using a tetragonal unit cells (NaNbNb₂O₇: $a \sim b = 5.483$ Å, $c = 20.911$ Å; NaNdTa₂O₇: $a \sim b = 5.469$ Å, $c = 21.134$ Å) consistent with distorted $n = 2$ Ruddlesden-Popper type structures. Again this contrasts previous reports of an undistorted ($I4/mmm$) structure for NaNbNb₂O₇.³⁵ We did not observe any evidence by diffraction for mixed cation (Na/Rb)NdNb₂O₇ or (Na/Rb)NdTa₂O₇ phases during the cation exchange reactions, with RbNdM₂O₇ starting materials converting directly to NaNdM₂O₇ product phases.

SHG measurements revealed that neither NaNbNb₂O₇ or NaNdTa₂O₇ are SHG active, indicating that both phases adopt centrosymmetric crystal structures. Given that it is possible for phases to be metrically tetragonal but described in an orthorhombic space group, our symmetry analysis (Table S1) indicates there are 12 possible centrosymmetric tetragonal or orthorhombic models for the NaNdM₂O₇ phases: *P4₂/mcm*, *P4₂/mnm*, *Pccm*, *Pbcb*, *Pbcm*, *Pnnm*, *Pnab*, *Pnam*, *Bbmm*, *Bbcm*, *Bmcm* and *Bbcb*. Again these are described with the stacking axis aligned along z .

Synchrotron X-ray diffraction data allow us to eliminate all the centered models on the basis of extinction conditions as shown in Figure S4. Further examination of the diffraction data show that the *P4₂/mcm*, *Pccm* and *Pbcm* structural models can be eliminated for NaNbNb₂O₇, and the *Pbcb* and *Pnab* models can be eliminated for both NaNbNb₂O₇ and NaNdTa₂O₇, which leaves only 3 candidate structural models for the NaNbNb₂O₇ (*P4₂/mnm*, *Pnnm* and *Pnam*) and 6 candidate structural models for the NaNdTa₂O₇ (*P4₂/mcm*, *P4₂/mnm*, *Pccm*, *Pbcm*, *Pnnm*, and *Pnam*).

In a direct analogy to the lithium phases, the sodium cations reside within 4-coordinate, pseudo-tetrahedral sites located between the perovskite double-layers, and can also adopt ordered or disordered configurations. In the structural model in space *Pnam*, the sodium cations reside on an 8*d* site which

must be half-occupied to respect the sample stoichiometry, and as a result the sodium cations are in a disordered configuration. In contrast, the model in space group *P4₂/mcm* has one 4*e*, one 2*b* and one 2*d* sodium site; *P4₂/mnm* has one 4*d* and one 4*e* sodium site; *Pccm* has one 2*e*, one 2*f*, one 2*g* and one 2*h* sodium site; *Pbcm* has two separate 4*c* sodium sites, and *Pnnm* has one 4*e* and one 4*f* sodium site allowing the sodium cations to adopt a range of ordered and disordered configurations in these five models.

Structural models were constructed in all the remaining candidate space groups and refined against the neutron powder diffraction data. During the refinements all atomic positional and displacement parameters were refined freely. The occupancies of the sodium sites were refined (within the constraint of the overall sample stoichiometry) to determine if the sodium cations were ordered or disordered, and it was observed that ordered sodium configurations gave superior fits for the *P4₂/mnm* and *Pnnm* models, while disordered sodium configurations gave superior fits for both the *P4₂/mcm*, *Pccm* and *Pbcm* models. NdNbO₄ was added as a second phase for the refinement of NaNbNb₂O₇.

Refinement of all models against the neutron powder diffraction data proceeded smoothly. Fitting statistics (Table 5) show that the models in space groups *Pnnm*, *Pnam* and *P4₂/mnm* achieve the best fits to the data for both NaNbNb₂O₇ and NaNdTa₂O₇. However close inspection of the fits using the *Pnam* models reveal these do not account for the intensity of the [114] and [112] diffraction peaks at 3.12Å and 3.63Å respectively, as shown in Figures S5 and S6 in the Supporting Information, indicating this model is incorrect.

The remaining two models *P4₂/mnm* ($a^-b^0c^0/b^0a^-c^0$) and *Pnnm* ($a^-b^-c^0/b^-a^-c^0$) describe similar octahedral tilting patterns, with the *P4₂/mnm* describing a special case of the *Pnnm* model in which the '*b*' tilt has zero magnitude. Close inspection of the atomic coordinates of the *Pnnm* models refined for NaNbNb₂O₇ and NaNdTa₂O₇ reveal O-O-O bond angles corresponding to '*a*' and '*b*' tilts are very different, and the magnitude of the '*b*' tilt is very close to zero, as shown in detail in Figure S7 in the supporting information. Given the similarity of the fitting statistics of the *P4₂/mnm* and *Pnnm* models and the small magnitude of the '*b*' tilt it is hard to differentiate between these two models on the basis of diffraction data alone.

Atom	site	<i>x</i>	<i>y</i>	<i>z</i>	<i>U</i> _{iso} (Å ³)
Na(1)	4e	0 <i>0</i>	0 <i>0</i>	0.2649(3) <i>0.26413</i>	0.0346(17)
Nd(1)	4f	0.2587(3) <i>0.26241</i>	0.2587(3) <i>0.26241</i>	0 <i>0</i>	0.0049(4)
Nb(1)	8j	0.2531(3) <i>0.25345</i>	0.2531(3) <i>0.25345</i>	0.3943(0) <i>0.39445</i>	0.0030(3)
O(1)	4g	0.8034(4) <i>0.80966</i>	0.8034(4) <i>0.80966</i>	½ <i>½</i>	0.0182(10)
O(2)	4e	½ <i>½</i>	½ <i>½</i>	0.5725(1) <i>0.57197</i>	0.0029(8)
O(3)	4e	0 <i>0</i>	0 <i>0</i>	0.6071(2) <i>0.60810</i>	0.0252(12)
O(4)	8h	½ <i>½</i>	0 <i>0</i>	0.4153(1) <i>0.41723</i>	0.0218(7)
O(5)	8j	0.7138(2) <i>0.71507</i>	0.7138(2) <i>0.71507</i>	0.6885(1) <i>0.68983</i>	0.0122(5)

NaNdNb₂O₇ – space group *P4₂/mnm* (#136)
Lattice parameters from experiment:
a = 5.4829(2) Å, *b* = 5.4829(2) Å, *c* = 20.9112(8) Å,
volume = 628.63(6) Å³
Lattice parameters from theory:
a = 5.48088 Å, *b* = 5.48088 Å, *c* = 20.80676 Å,
volume = 625.04 Å³
Formula weight: 465.04 g mol⁻¹, *Z* = 4
Radiation source: Neutron Time of flight
Temperature: 298 K
χ² = 8.56, wRp = 4.79%, Rp = 4.82%

Table 6. Parameters from the structural refinement of NaNdNb₂O₇ against neutron powder diffraction data collected at 298 K compared to structural data from our first-principles calculations. For each atomic species, the first row of fractional coordinates corresponds to experimental data (with the corresponding isotropic displacement parameter), whereas the second row (italic) is from our DFT calculations.

DFT calculations confirm that *P4₂/mnm* is more stable than *Pnnm*. The energy difference between the two phases in the case of NaNdNb₂O₇ is less than 0.05 meV/formula unit, suggesting that the two structures are likely identical within the calculation precision. This is confirmed by close inspection of the relaxed structures, revealing that the optimized *Pnnm* model has essentially zero *b* tilt, consistent with *P4₂/mnm* symmetry. This also happens for NaNdT_aO₇, however the *Pnnm* structure ends up more stable than *P4₂/mnm* by less than 1 meV/formula unit. Given the tiny energy difference between the two structures and the fact that the *Pnnm* model relaxes to *P4₂/mnm*, we conclude that the best and simplest description of the structures of NaNdNb₂O₇ and NaNdT_aO₇ are given by the *P4₂/mnm* models.

Observed calculated and difference plots from the refinement of *P4₂/mnm* symmetry models against neutron powder diffraction data are shown in Figures S8 and S9. Complete descriptions of the refined structures of NaNdNb₂O₇ and NaNdT_aO₇ detailed in Tables 6 and 7 respectively, with selected bond lengths in Table 8. Parameters from the relaxed computational structures of NaNdNb₂O₇ and NaNdT_aO₇ are shown in Tables 6 and 7, again showing excellent agreement with the experimentally determined structures.

Atom	site	<i>x</i>	<i>y</i>	<i>z</i>	<i>U</i> _{iso} (Å ³)
Na(1)	4e	0 <i>0</i>	0 <i>0</i>	0.2608(4) <i>0.26205</i>	0.0427(17)
Nd(1)	4f	0.2569(3) <i>0.26326</i>	0.2569(3) <i>0.26326</i>	0 <i>0</i>	0.0043(4)
Ta(1)	8j	0.2543(3) <i>0.25327</i>	0.2543(3) <i>0.25327</i>	0.3957(1) <i>0.39503</i>	0.0050(3)
O(1)	4g	0.8009(4) <i>0.80697</i>	0.8009(4) <i>0.80697</i>	½ <i>½</i>	0.0130(9)
O(2)	4e	½ <i>½</i>	½ <i>½</i>	0.5742(2) <i>0.57203</i>	0.0101(9)
O(3)	4e	0 <i>0</i>	0 <i>0</i>	0.6020(2) <i>0.60541</i>	0.0352(15)
O(4)	8h	½ <i>½</i>	0 <i>0</i>	0.4160(1) <i>0.41761</i>	0.0216(7)
O(5)	8j	0.7181(3) <i>0.71783</i>	0.7181(3) <i>0.71783</i>	0.6883(1) <i>0.68968</i>	0.0099(5)

NaNdT_aO₇ – space group *P4₂/mnm* (#136)
Lattice parameters from experiment:
a = 5.4686(2) Å, *b* = 5.4686(2) Å, *c* = 21.1345(9) Å,
volume = 632.03(7) Å³
Lattice parameters from theory:
a = 5.48525 Å, *b* = 5.48525 Å, *c* = 20.94628 Å,
volume = 630.23 Å³
Formula weight: 641.12 g mol⁻¹, *Z* = 4
Radiation source: Neutron Time of flight
Temperature: 298 K
χ² = 6.96, wRp = 4.13%, Rp = 3.98%

Table 7. Parameters from the structural refinement of NaNdT_aO₇ against neutron powder diffraction data collected at 298 K compared to structural data from our first-principles calculations. For each atomic species, the first row of fractional coordinates corresponds to experimental data (with the corresponding isotropic displacement parameter), whereas the second row (italic) is from our DFT calculations.

Cation	Anion	NaNdNb ₂ O ₇		NaNdT _a O ₇	
		Length (Å)	BVS	Length (Å)	BVS
Na(1)	O(5) × 2	2.303(5)	0.88	2.279(6)	0.91
	O(5) × 2	2.424(4)		2.431(5)	
Nd(1)	O(1) × 2	2.413(4)	2.96	2.430(3)	2.95
	O(1) × 2	3.092(4)		3.060(3)	
	O(2) × 2	2.514(3)		2.531(3)	
	O(3) × 2	2.918(4)		2.860(5)	
	O(4) × 4	2.627(3)		2.625(3)	
Nb/Ta(1)	O(1)	2.253(1)	5.15	2.245(1)	5.21
	O(2)	2.036(2)		2.004(3)	
	O(3)	1.963(2)		1.967(2)	
	O(4) × 2	1.988(2)		1.981(2)	
	O(5)	1.750(2)		1.788(2)	

Table 8. Selected bond lengths from the structures of NaNdNb₂O₇ and NaNdT_aO₇ refined in space group *P4₂/mnm*.

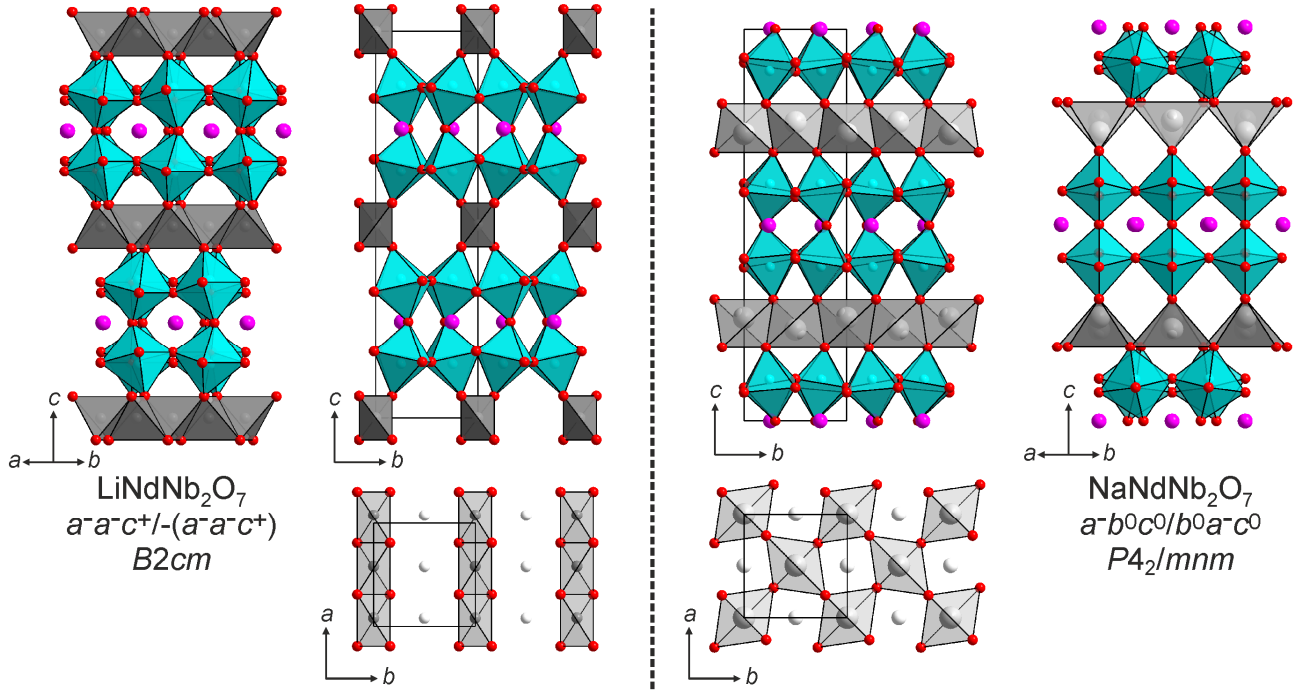


Figure 3. The structures of $\text{LiNdNb}_2\text{O}_7$ (left) and $\text{NaNbNb}_2\text{O}_7$ (right). Purple, blue, red, dark-grey and light-grey spheres represent Nd, Nb, O, Li and Na respectively. White spheres indicate the positions of empty $\text{A}'\text{O}_4$ sites.

Discussion

The crystal structures of LiNdM_2O_7 and $\text{NaNbNb}_2\text{O}_7$ ($M = \text{Nb, Ta}$) differ in two key respects: i) the tilting distortion of the MO_6 network and ii) the ordering of the Li and Na cations within the inter-layer tetrahedral coordination sites.

Considering the tilting distortions first, as noted above, the collective rotations of the connected MO_6 octahedra in perovskite lattices occur in response to a size mismatch between the average B-O bond lengths ($B = \text{Nb, Ta}$) and the A-O and A' -O lengths ($A = \text{Nb, Ta}$; $\text{A}' = \text{Li, Na}$) as these low-energy structural deformations allow the A-O and A' -O lengths to contract without changing the B-O length. The magnitude of the cation size mismatch can be conveniently parameterized in the case of the 12-coordinate A-cations using the Goldschmidt tolerance factor, $t = \langle \text{A-O} \rangle / (\sqrt{2} \langle \text{B-O} \rangle)$.⁵⁷ Using tabulated ionic radii ($\text{Nd}^{3+} = 1.27 \text{ \AA}$; $\text{Nb}^{5+} = 0.64 \text{ \AA}$; $\text{O} = 1.40 \text{ \AA}$)⁵⁸ a value of $t = 0.925$ can be determined for the NdNb_2O_7 perovskite sheets, indicating this double-layer will have a strong geometric drive to adopt a significantly distorted configuration in the absence of any influence from the A' -cations. It should also be noted that the 6-coordinate ionic radius of Ta^{5+} is also 0.64 \AA , thus it is no surprise that the corresponding niobium and tantalum phases are isostructural.

It is also possible to formulate a tolerance factor, t' , for the A' tetrahedral cation sites, by considering the $\langle \text{B-O} \rangle$ and $\langle \text{A}'\text{-O} \rangle$ bond lengths of the undistorted aristotype framework, as described in detail in the supporting information (Figure S10), as $t' = \langle \text{A}'\text{-O} \rangle / [(\sqrt{3}/\sqrt{2}) \langle \text{B-O} \rangle]$. Utilizing the tabulated 4-coordinate ionic radii of Li^+ (0.59 \AA) and Na^+ (0.99 \AA) we can obtain values of $t' = 0.796$ and $t' = 0.956$ for Li/Nb and Na/Nb respectively. The significantly smaller value of t' for the Li/Nb combination compared to the Na/Nb combination provides a simple explanation for the differing tilting patterns of the Li and Na phases, however close inspection of the crystal structures reveals more subtle drivers.

Calculating BVS values for the Na^+ cations in the refined structures of $\text{NaNbNb}_2\text{O}_7$ and $\text{NdNbTa}_2\text{O}_7$ (Table 8) reveals that in both structures the Na cations are ‘under bonded’ ($\text{BVS Na}_{\text{Nb}} = 0.88$; $\text{Na}_{\text{Ta}} = 0.91$) indicating that the 4-coordinate Na sites are larger than ideal. In contrast the BVS values for the Li^+ cations in $\text{LiNdNb}_2\text{O}_7$ and $\text{LiNdTa}_2\text{O}_7$ (Table 4) are close to ideal ($\text{BVS Li}_{\text{Nb}} = 0.99$; $\text{Li}_{\text{Ta}} = 0.98$). This indicates that the tilting distortions of the lithium containing phases have optimized the size of the Li coordination sites, while the corresponding distortions of the Na-containing phases have not optimized the Na sites. Why the difference?

Figure 3 shows that the sodium cations order within the inter-layer cations sites to form a network of corner-linked NaO_4 tetrahedra. This arrangement minimizes Na-Na repulsions in line with Pauling’s third crystallographic rule.⁵⁹ However a feature of this arrangement is that it is not possible to contract the average Na-O bond length via octahedral tilting as the displacement of an oxide ion to shorten one Na-O length necessarily elongates another, and as a result the average Na-O distance does not change but the average O-O separation declines making large angle tilts unfavourable. The only mechanism which allows a contraction of the average Na-O bond length is to shrink the inter-layer separation, but again this also shrinks the average O-O separation so can only occur to a limited extent. Thus it can be seen that the small magnitude of the MO_6 tilting distortion observed for the NaNbM_2O_7 phases, and thus the under bonding of the Na cations, is a consequence of the Na cation ordering scheme, suggesting that in this instance minimizing Na-Na repulsion is energetically more important than optimizing the size of the A' coordination sites.

These same factors (minimizing A' - A' repulsion vs optimizing the size of the A' coordination site) are also operative in determining the structure of the LiNdM_2O_7 phases, however the smaller size of the Li^+ cation means that a different balance is struck. Figure 3 shows that the lithium cations order within

the inter-layer cations sites of the LiNdM_2O_7 phases to form chains of edge-linked LiO_4 tetrahedra. This is a less optimal configuration with respect to minimizing $\text{A}'\text{-A}'$ repulsion than the corner-linked configuration adopted in the sodium phases. However, this edge-shared connectivity allows the tilting distortions of the MO_6 network to decrease the size of the occupied tetrahedral cation sites and optimize the coordinations of the A' cations, resulting in a near ideal coordination environment for the Li cations. Thus we propose that the differing structures adopted by the NaNdM_2O_7 and LiNdM_2O_7 phases arise from a competition between minimizing the $\text{A}'\text{-A}'$ repulsion and optimizing the A' -cation coordination site, with the former being the dominant factor for the Na phases and the latter for the Li phases.

This idea can be supported by examining the energy minimized, hypothetical structures of the Na and Li phases with the alternate structure type. That is to say $\text{NaNdNb}_2\text{O}_7$ with a $B2cm$ symmetry structure and $\text{LiNdNb}_2\text{O}_7$ with a $P4_2/mnm$ structure. As shown in Tables S4 and S5, the energy minimized, hypothetical $B2cm$ structure of $\text{NaNdNb}_2\text{O}_7$ adopts a much more distorted MO_6 framework than the experimental structure. This increased distortion acts to contract the size of the Na coordination site raising the Na BVS to a value of +1.23. However despite this improvement to the local Na-O bonding, this $B2cm$ configuration is 88 meV/formula unit less stable than an equivalent, energy minimized structure with $P4_2/mnm$ symmetry. This is consistent with the idea that unfavorable increase Na-Na repulsion, which occurs when the Na cations are arranged in an edge-sharing configuration within the $B2cm$ structure, outweighs the improved Na-O bonding arising from contraction of the Na coordination site, making the $P4_2/mnm$ symmetry structure the optimal configuration for $\text{NaNdNb}_2\text{O}_7$.

Similarly, inspection of the energy minimized, hypothetical $P4_2/mnm$ symmetry structure for $\text{LiNdNb}_2\text{O}_7$ (Tables S6 and S7) reveals it is 289 meV/formula unit less stable than the equivalent energy minimized $B2cm$ phase. This lower stability can be attributed to the significant expansion of the Li coordination site which occurs on switching to the $P4_2/mnm$ symmetry structure. The resulting BVS value for Li (0.73) in this site is too small to be chemically sensible, indicating this site is much too large to accommodate Li^+ (it is essentially only three-coordinate), consistent with the proposal that optimizing the size of the Li coordination site has a larger impact on the energy of LiNdM_2O_7 phases than the increase Li-Li repulsion arising from the edge-sharing of LiO_4 units, making the $B2cm$ symmetry structure the optimal configuration for $\text{LiNdNb}_2\text{O}_7$.

Conclusion

The contrasting balance between minimizing the $\text{A}'\text{-A}'$ cation repulsions and optimizing the A' coordination reached by the lithium and sodium phases has echoes of the similar balance in the $\text{A}'\text{NdM}_2\text{O}_7$ ($\text{A}' = \text{Rb}, \text{Cs}$) Dion-Jacobson phases between minimizing O-O repulsion and optimizing the A' coordination.²⁸ Together these observations suggest that the tilting distortions of $\text{A}'\text{AB}_2\text{O}_7$ phases with either Ruddlesden-Popper or Dion-Jacobson frameworks can be tuned by careful selection of the A' cation. This feature is further emphasized by observing that in order for the tilting distortions of the MO_6 network to contract the lithium coordination site uniformly, the x and y tilts in adjacent perovskite double sheets have to have the opposite sign, ie. $a^p b^q c^r / -(a^p b^q) \pm c^r$. Thus it can be seen that the small size of the lithium cations directs the lattice into the polar $a^-a^-c^+ / -(a^-a^-c^+)$ tilting distortion. It therefore

seems likely that by careful selection of A' cations, a series of novel polar configurations can be constructed.

ASSOCIATED CONTENT

Supporting Information. Symmetry analysis of $n = 2$ Ruddlesden-Popper phases; Extinction conditions of LiNdM_2O_7 and NaNdM_2O_7 phases; Comparison of constrained and unconstrained $P2cm$ models of LiNdM_2O_7 phases; Fitted neutron powder diffraction data from the refinement of LiNdM_2O_7 and NaNdM_2O_7 phases; Tolerance factor analysis for tetrahedral A' -cation site; Energy minimized structures of hypothetical $B2cm$ symmetry $\text{NaNdNb}_2\text{O}_7$ and $P4_2/mnm$ symmetry $\text{LiNdNb}_2\text{O}_7$. This material is available free of charge via the Internet at <http://pubs.acs.org>.

AUTHOR INFORMATION

Corresponding Author

michael.hayward@chem.ox.ac.uk
nbenedek@cornell.edu

Author Contributions

The manuscript was written through contributions of all authors.

Funding Sources

Any funds used to support the research of the manuscript should be placed here (per journal style).

ACKNOWLEDGMENT

Experiments at the Diamond Light Source were performed as part of the Block Allocation Group award "Oxford Solid State Chemistry BAG to probe composition-structure-property relationships in solids" (EE13284). Experiments at the ISIS pulsed neutron facility were supported by a beam time allocation from the STFC (RB1620305). NAB was supported by the National Science Foundation (NSF) via Grant DMR-1550347. GK was supported by the NSF via Grant DMR-1719875. DMH was supported by an NSF Graduate Research Fellowship. This work used the high-performance computing facilities of the Cornell Center for Advanced Computing. WZ and PSH thank the Welch Foundation (Grant E-1457) and the NSF (DMR-1503573) for support.

REFERENCES

1. Lines, M. E.; Glass, A. M., *Principles and Applications of Ferroelectrics and Related Materials*. Oxford University Press: Oxford, 1991.
2. Nye, F. J., *Physical Properties of Crystals*. Oxford University Press: Oxford, UK, 1957.
3. Halasyamani, P.; Poeppelmeier, K. R., Noncentrosymmetric oxides. *Chem. Mater.* **1998**, *10*, 2753-2769.
4. Cohen, R. E., Origin of Ferroelectricity in Perovskite Oxides. *Nature* **1992**, *358*, 136-138.
5. Kang, S. K.; Tang, H.; Albright, T. A., Structures for $d^0 \text{ML}_6$ and ML_5 Complexes. *J. Am. Chem. Soc.* **1993**, *115*, 1971-1981.
6. Kunz, M.; Brown, I. D., Out-of-Center Distortions around Octahedrally Coordinated d^0 Transition-Metals. *J. Solid State Chem.* **1995**, *115*, 395-406.
7. Pearson, R. G., The 2nd-Order Jahn-Teller Effect. *Theochem-Journal of Molecular Structure* **1983**, *12*, 25-34.
8. Lefebvre, I.; Lannoo, M.; Allan, G.; Ibanez, A.; Fourcade, J.; Jumas, J. C.; Beaurepaire, E., Electronic-Properties of Antimony Chalcogenides. *Phys. Rev. Lett.* **1987**, *59*, 2471-2474.
9. Lefebvre, I.; Szymanski, M. A.; Olivier-Fourcade, J.; Jumas, J. C., Electronic Structure of Tin Monochalcogenides from SnO to SnTe . *Phys. Rev. B* **1998**, *58*, 1896-1906.
10. Seshadri, R.; Hill, N. A., Visualizing the Role of Bi 6s "Lone Pairs" in the Off-Center Distortion in Ferromagnetic BiMnO_3 . *Chem. Mater.* **2001**, *13*, 2892-2899.

11. Stoltzfus, M. W.; Woodward, P. M.; Seshadri, R.; Klepeis, J. H.; Bursten, B., Structure and Bonding in SnWO_4 , PbWO_4 , and BiVO_4 : Lone Pairs vs Inert Pairs. *Inorg. Chem.* **2007**, *46*, 3839-3850.
12. Watson, G. W.; Parker, S. C., Origin of the Lone Pair of $\alpha\text{-PbO}$ from Density Functional Theory Calculations. *J. Phys. Chem. B* **1999**, *103*, 1258-1262.
13. Watson, G. W.; Parker, S. C.; Kresse, G., Ab Initio Calculation of the Origin of the Distortion of $\alpha\text{-PbO}$. *Phys. Rev. B* **1999**, *59*, 8481-8486.
14. Hill, N. A., Why Are There So Few Magnetic Ferroelectrics. *J. Phys. Chem. B* **2000**, *104*, 6694-6709.
15. Benedek, N. A.; Fennie, C. J., Hybrid Improper Ferroelectricity: A Mechanism for Controllable Polarization-Magnetization Coupling. *Phys. Rev. Lett.* **2011**, *106*, 107204.
16. Mulder, A. T.; Benedek, N. A.; Rondinelli, J. M.; Fennie, C. J., Turning ABO_3 Antiferroelectrics into Ferroelectrics: Design Rules for Practical Rotation-Driven Ferroelectricity in Double Perovskites and $\text{A}_3\text{B}_2\text{O}_7$ Ruddlesden-Popper Compounds. *Advanced Functional Materials* **2013**, *23*, 4810-4820.
17. Benedek, N. A.; Mulder, A. T.; Fennie, C. J., Polar octahedral rotations: A path to new multifunctional materials. *J. Solid State Chem.* **2012**, *195*, 11-20.
18. Bousquet, E.; Dawber, M.; Stucki, N.; Lichtensteiger, C.; Hermet, P.; Gariglio, S.; Triscone, J. M.; Ghosez, P., Improper Ferroelectricity in Perovskite Oxide Artificial Superlattices. *Nature* **2008**, *452*, 732-U4.
19. Benedek, N. A.; Rondinelli, J. M.; Djani, H.; Ghosez, P.; Lightfoot, P., Understanding Ferroelectricity in Layered Perovskites: New Ideas and Insights From Theory and Experiments. *Dalton Trans.* **2015**, *44*, 10543-10558.
20. Bostrom, H. L. B.; Senn, M. S.; Goodwin, A. L., Recipes for improper ferroelectricity in molecular perovskites. *Nature Communications* **2018**, *9*, 1-7.
21. Young, J.; Stroppa, A.; Picozzi, S.; Rondinelli, J. M., Anharmonic lattice interactions in improper ferroelectrics for multiferroic design. *J. Phys.:Condens. Matter* **2015**, *27*, 283202.
22. Oh, Y. S.; Luo, X.; Huang, F. T.; Wang, Y. Z.; Cheong, S. W., Experimental demonstration of hybrid improper ferroelectricity and the presence of abundant charged walls in $(\text{Ca}, \text{Sr})_3\text{Ti}_2\text{O}_7$ crystals. *Nat. Mater.* **2015**, *14*, 407-413.
23. Liu, M. F.; Zhang, Y.; Lin, L. F.; Lin, L.; Yang, S. W.; Li, X.; Wang, Y.; Li, S. Z.; Yan, Z. B.; Wang, X. Z.; Li, X. G.; Dong, S.; Liu, J. M., Direct observation of ferroelectricity in $\text{Ca}_3\text{Mn}_2\text{O}_7$ and its prominent light absorption. *Appl. Phys. Lett.* **2018**, *113*, 022902.
24. Yoshida, S.; Fujita, K.; Akamatsu, H.; Hernandez, O.; Sen Gupta, A.; Brown, F.; Padmanabhan, H.; Gibbs, A. S.; Kuge, T.; Tsuji, R.; Murai, S.; Rondinelli, J. M.; Gopalan, V.; Tanaka, K., Ferroelectric $\text{Sr}_3\text{Zr}_2\text{O}_7$: Competition between Hybrid Improper Ferroelectric and Antiferroelectric Mechanisms. *Advanced Functional Materials* **2018**, *28*, 1801856.
25. Dion, M.; Ganne, M.; Tournoux, M., The New Phase Families $\text{M}^{\text{II}}\text{Nb}_3\text{O}_{10}$ with Perovskite Sheets. *Mater. Res. Bull.* **1981**, *16*, 1429-1435.
26. Jacobson, A. J.; Johnson, J. W.; Lewandowski, J. T., Interlayer Chemistry between Thick Transition-Metal Oxide Layers - Synthesis and Intercalation Reactions of $\text{K}[\text{Ca}_2\text{Na}_{n-3}\text{Nb}_n\text{O}_{3n+1}]$ ($3 < n < 7$). *Inorg. Chem.* **1985**, *24*, 3727-3729.
27. Benedek, N. A., Origin of Ferroelectricity in a Family of Polar Oxides: The Dion-Jacobson Phases. *Inorg. Chem.* **2014**, *53*, 3769-3777.
28. Zhu, T.; Cohen, T.; Gibbs, A. S.; Zhang, W. G.; Halasyamani, P. S.; Hayward, M. A.; Benedek, N. A., Theory and Neutrons Combine To Reveal a Family of Layered Perovskites without Inversion Symmetry. *Chem. Mater.* **2017**, *29*, 9489-9497.
29. Strayer, M. E.; Gupta, A. S.; Akamatsu, H.; Lei, S.; Benedek, N. A.; Gopalan, V.; Mallouk, T. E., Emergent Noncentrosymmetry and Piezoelectricity driven by oxygen octahedral rotations in $n = 2$ Dion-jacobson phase layered perovskites. *Advanced Functional Materials* **2016**, *26*, 1930-1937.
30. Schaak, R. E.; Mallouk, T. E., Perovskites by design: A toolbox of solid-state reactions. *Chem. Mater.* **2002**, *14*, 1455-1471.
31. Hayward, M. A., Soft chemistry synthesis of oxides. In *Comprehensive Inorganic Chemistry II*, Reedijk, J.; Poeppelemeier, K. R., Eds. Elsevier: Oxford, 2013; Vol. 2, pp 417-453.
32. Ranmohotti, K. G. S.; Josepha, E.; Choi, J.; Zhang, J. X.; Wiley, J. B., Topochemical Manipulation of Perovskites: Low-Temperature Reaction Strategies for Directing Structure and Properties. *Adv. Mater.* **2011**, *23*, 442-460.
33. Gopalakrishnan, J.; Bhat, V.; Raveau, B., $\text{A}^{\text{I}}\text{LaNb}_2\text{O}_7$ - a New Series of Layered Perovskites Exhibiting Ion-Exchange and Intercalation Behavior. *Mater. Res. Bull.* **1987**, *22*, 413-417.
34. Toda, K.; Sato, M., Synthesis and structure determination of new layered perovskite compounds, $\text{ALaTa}_2\text{O}_{10}$ and $\text{ACa}_2\text{Ta}_3\text{O}_{10}$ ($\text{A}=\text{Rb}, \text{Li}$). *J. Mater. Chem.* **1996**, *6*, 1067-1071.
35. Josepha, E. A.; Farooq, S.; Mitchell, C. M.; Wiley, J. B., Synthesis and thermal stability studies of a series of metastable Dion-Jacobson double-layered neodymium-niobate perovskites. *J. Solid State Chem.* **2014**, *216*, 85-90.
36. Mahler, C. H.; Cushing, B. L.; Lalena, J. N.; Wiley, J. B., Divalent ion exchange of alkaline-earth cations into the triple-layered perovskite $\text{RbCa}_2\text{Nb}_3\text{O}_{10}$. *Mater. Res. Bull.* **1998**, *33*, 1581-1586.
37. Kodenkandath, T. A.; Kumbhar, A. S.; Zhou, W. L.; Wiley, J. B., Construction of copper halide networks within layered perovskites. Syntheses and characterization of new low-temperature copper oxyhalides. *Inorg. Chem.* **2001**, *40*, 710-714.
38. Kodenkandath, T. A.; Lalena, J. N.; Zhou, W. L. L.; Carpenter, E. E.; Sangregorio, C.; Falster, A. U.; Simmons, W. B.; O'Connor, C. J.; Wiley, J. B., Assembly of metal-anion arrays within a perovskite host. Low-temperature synthesis of new layered copper-oxyhalides, $(\text{CuX})\text{LaNb}_2\text{O}_7$, $\text{X} = \text{Cl}, \text{Br}$. *J. Am. Chem. Soc.* **1999**, *121*, 10743-10746.
39. Ranmohotti, K. G. S.; Montasserasadi, M. D.; Choi, J.; Yao, Y.; Mohanty, D.; Josepha, E. A.; Adireddy, S.; Caruntu, G.; Wiley, J. B., Room temperature oxidative intercalation with chalcogen hydrides: Two-step method for the formation of alkali-metal chalcogenide arrays within layered perovskites. *Mater. Res. Bull.* **2012**, *47*, 1289-1294.
40. Suzuki, H.; Notsu, K.; Takeda, Y.; Sugimoto, W.; Sugahara, Y., Reactions of alkoxyl derivatives of a layered perovskite with alcohols: Substitution reactions on the interlayer surface of a layered perovskite. *Chem. Mater.* **2003**, *15*, 636-641.
41. Takeda, Y.; Momma, T.; Osaka, T.; Kuroda, K.; Sugahara, Y., Organic derivatives of the layered perovskite $\text{HLaNb}_2\text{O}_7 \cdot x\text{H}_2\text{O}$ with polyether chains on the interlayer surface: characterization, intercalation of LiClO_4 , and ionic conductivity. *J. Mater. Chem.* **2008**, *18*, 3581-3587.
42. Takeda, Y.; Suzuki, H.; Notsu, K.; Sugimoto, W.; Sugahara, Y., Preparation of a novel organic derivative of the layered perovskite bearing $\text{HLaNb}_2\text{O}_7 \cdot n\text{H}_2\text{O}$ interlayer surface trifluoroacetate groups. *Mater. Res. Bull.* **2006**, *41*, 834-841.
43. Sato, M.; Abo, J.; Jin, T., Structure examination of $\text{NaLaNb}_2\text{O}_7$ synthesized by soft chemistry. *Solid State Ionics* **1992**, *57*, 285-293.
44. Larson, A. C.; Von Dreele, R. B. *General Structure Analysis System*, Los Alamos National Laboratory Report LAUR 86-748: 2000.
45. Ok, K. M.; Chi, E. O.; Halasyamani, P. S., Bulk characterization methods for non-centrosymmetric materials: second-harmonic generation, piezoelectricity, pyroelectricity, and ferroelectricity. *Chem. Soc. Rev.* **2006**, *35*, 710-717.
46. Perdew, J. P.; Ruzsinszky, A.; Csonka, G. I.; Vydrov, O. A.; Scuseria, G. E.; Constantin, L. A.; Zhou, X. L.; Burke, K., Restoring the density-gradient expansion for exchange in solids and surfaces. *Phys. Rev. Lett.* **2008**, *100*, 136406.
47. Blochl, P. E., Projector augmented-wave method. *Phys. Rev. B* **1994**, *50*, 17953-17979.
48. Kresse, G.; Joubert, D., From ultrasoft pseudopotentials to the projector augmented-wave method. *Phys. Rev. B* **1999**, *59*, 1758-1775.
49. Kresse, G.; Hafner, J., Ab-initio molecular-dynamics for liquid-metals. *Phys. Rev. B* **1993**, *47*, 558-561.
50. Kresse, G.; Furthmüller, J., Efficient iterative schemes for ab initio total-energy calculations using a plane-wave basis set. *Phys. Rev. B* **1996**, *54*, 11169-11186.

51. Kresse, G.; Furthmüller, J., Efficiency of ab-initio total energy calculations for metals and semiconductors using a plane-wave basis set. *Computational Materials Science* **1996**, *6*, 15-50.
52. Kresse, G.; Hafner, J., Ab-initio Molecular Dynamics Simulation of the Liquid-metal Amorphous-semiconductor Transition in Germanium. *Phys. Rev. B* **1994**, *49*, 14251-14269.
53. Aleksandrov, K. S.; Bartolome, J., Octahedral Tilt Phases in Perovskite-like Crystals with Slabs Containing an Even Number of Octahedral Layers. *J. Phys.:Condens. Matter* **1994**, *6*, 8219-8235.
54. Campbell, B. J.; Stokes, H. T.; Tanner, D. E.; Hatch, D. M., ISODISPLACE: a web-based tool for exploring structural distortions. *J. Appl. Crystallogr.* **2006**, *39*, 607-614.
55. Brese, N. E.; O'Keeffe, M., Bond-Valence Parameters for Solids. *Acta Crystallogr., Sect. B : Struct. Sci.* **1991**, *B47*, 192-197.
56. Brown, I. D.; Altermatt, D., Bond-Valence Parameters Obtained from a Systematic Analysis of the Inorganic Crystal Structure Database. *Acta Crystallogr., Sect. B : Struct. Sci.* **1985**, *B41*, 244-247.
57. Goldschmidt, V. M., Die Gesetze der Krystallochemie. *Naturwissenschaften* **1926**, *14*, 477-485.
58. Shannon, R. D., Revised effective ionic radii. *Acta Cryst.* **1976**, *A32*, 751-766.
59. Pauling, L., The Principles Determining the Structure of Complex Ionic Crystals. *J. Am. Chem. Soc.* **1929**, *51*, 1010-1026.

